RSC Advances

PAPER

View Article Online
View Journal | View Issue

Cite this: *RSC Adv.*, 2022, **12**, 34640

Fabrication of $TiVO_4$ photoelectrode for photoelectrochemical application†

Manal Alruwaili, *[ab] Anurag Roy, [a] Srijita Nundy[a] and Asif Ali Tahir *[a]

Photoelectrochemical (PEC) water splitting is one of the promising, environmentally friendly, carbon emission-free strategies for the cost-effective production of hydrogen. The interest in developing effective approaches for solar-to-hydrogen production with stable and visible light active semiconductors directed many researchers to develop stable and efficient materials. For the first time, a nanostructured $TiVO_4$ photoanode was fabricated at a substrate temperature of 250 °C and further annealed at 600 °C using the spray pyrolysis technique and it obtained an optical band gap of ~2.18 eV. The photoanode underwent photoelectrochemical testing, where it exhibited a high photocurrent density of 0.080 mA cm^{-2} at 1.23 V (*vs.* reversible hydrogen electrode), which can be stable up to 110 min. Further, various physicochemical characterizations were employed to understand the phase purity and thin film growth mechanism. A systematic substrate and annealed temperatures were monitored during the fabrication process. The transmission electron microscopy (TEM) studies revealed agglomeration of $TiVO_4$ nanoparticles with an average size of ~100 nm accompanying dendritic orientation at the outer edge. This study envisages the design and development of a novel photocatalyst for water splitting under visible light irradiation, an ideal route to a cost-effective, large-scale, sustainable route for hydrogen production.

Received 18th September 2022
Accepted 24th November 2022

DOI: 10.1039/d2ra05894d

rsc.li/rsc-advances

1. Introduction

The most incredible mission of the current scientific generation is to address the considerable energy demands.[1] Researchers are devoting their efforts to searching for secure, safe, and sustainable energy options to cope with expected nonrenewable energy shortages and eliminate environmental pollutants. Solar energy is expected to be the leading and safe option that can solve the energy crisis, targeted explicitly through improvements to ensure access to reliable, sustainable, affordable and modern energy. An understanding of renewable-energy solutions for water splitting, which is the process of hydrogen production by direct water decomposition, heavily depends on further developments in cost-effectiveness and environmental technologies. The photoelectrochemical (PEC) water splitting is considered one of the most promising H_2 generation methods with required potential ($\Delta G^\circ = 237$ kJ mol^{-1}), due to its use of the unlimited energy source of solar light without producing any CO_2.[2–5] Since 1972, after the pioneering work by Fujishima and Honda using TiO_2 as a photocatalyst in a water splitting system.[6] To achieve high performance of PEC materials, suitable band gap, diffusion length, bulk defects and surface recombination, *i.e.* accessible surface area, porosity, pore volume and high crystallinity, are critical parameters to affect the overall PEC performance.[7] Particularly, porosity and pore fall into the requirements for low diffusion length materials, such as some metal oxides.[8–10]

Fe_2O_3,[11] Co_3O_4,[12] TiO_2,[13] MoO_x [14] and VO_2 [15] are materials that have been used widely in PEC applications, but some drawbacks suppress their work, such as fast charge carriers recombination and low charge transport. In addition, these semiconductors' band edge potentials are incompatible with the redox potentials for some specific photocatalytic redox reactions. Hence, if these bimetallic semiconductors can be combined with other novel photoactive materials such as NiO,[16] ZnO,[17] CdO (ref. 18) *etc.*, to construct heterojunctions such as Co_3O_4/TiO_2,[19] $Fe_2O_3/Au/TiO_2$,[20] ZnO/Fe_2O_3,[21] Fe_2O_3/CdO,[22] MoO_x/GaP [23] and ZnO/NiO [24] *etc.* with proper band alignment, they could serve as efficient PEC material as compared to single-phase metal oxide. It can be combined with other dopants to extend those materials' spectral response towards visible light.[25–27]

Recently, bimetallic oxide materials ($BiVO_4$,[28] $Fe_xV_xO_4$,[29] $Cu_xV_xO_x$ [30] have become promising photoelectrode due to their tuned bandgap, suitable for PEC water splitting. They have shown an effective usage of solar irradiation owing to their synergic absorption in the visible and ultraviolet (UV) regions.[23,31] Numerous pioneering reports highlighted the

[a]*Environment and Sustainability Institute, Faculty of Environment, Science and Economy, University of Exeter, Penryn TR10 9FE, UK. E-mail: ma942@exeter.ac.uk; a.tahir@exeter.ac.uk*

[b]*Physics Department, Faculty of Science, Jouf University, PO Box 2014, Sakaka 42421, Saudi Arabia*

† Electronic supplementary information (ESI) available. See DOI: https://doi.org/10.1039/d2ra05894d

superior performance of TiV systems as composites VO_x/TiO_2 or as doping compared to $TiVO_4$ – bimetal oxide on their plausible photocatalysis application.[32,33] Samdarshi *et al.* (2010) evaluated the effect of silver on the titanium vanadium mixed metal (Ag/TiV) oxides.[34] They observed that the system could absorb a large portion of the visible spectrum, where favourable electron transfer could be experienced anatase-rutile mixed phase where silver dominated through its scavenging action to reduce hole recombination. On the other hand, the Ag-doped TiV films were developed by the sol–gel technique, increasing antibacterial activity when exposed to visible light.[35] The visible transmittance can be substantially improved, resulting in a higher photocatalytic property under visible light irradiation for the Ti–V system.[36] Alternatively, an efficient way to use the majority of sunlight could be achieved using nanocomposite semiconductors such as TiO_2–V_2O_5.[37] Li *et al.* (2016) investigated V^{4+} ion doping to decorate TiO_2 nanocrystals, which tailored energy level alingment of TiO_2 nanostructure by shortening the electronic transfer lifetime to 34.7% compared to only TiO_2.[38] By contrast, no reports have gone on to utilize TiV systems in PEC applications. Extending these advanced characteristics to PEC systems will undoubtedly bring breakthroughs in PEC-driven photo-to-energy conversions. The main challenge now is to design optical paths to achieve high light absorption with high activity, durability, and selectivity during the PEC analysis.

Single-phase $TiVO_4$ is still not explored much and received little attention, which can promise effective PEC characteristics reported by various TiV systems. Comparing $TiVO_4$ to TiO_2, its interfacial structure is superior for higher electron diffusion during high-temperature fabrication, creating a low impedance contact possessing high optical transparency and providing long-term stability. By comparing the requirements of novel PEC materials, $TiVO_4$ can be achieved with similar small-radius cations, which are directed to narrow band gap and have transition metals as the cation component, which is earth-abundant, cost-effective, and low-toxicity, benefiting wide usage in the future.

This work synthesized a phase pure $TiVO_4$ as a photoanode using the scalable spray pyrolysis technique. The photoanode produced by spray pyrolysis has a large surface area of substrate coverage potential, a cost-effective method and homogeneity of mass synthesis. The influence of the thin films' substrate and annealing temperatures is further studied and exhibited remarkable hierarchical structures. Furthermore, the spray pyrolyzed $TiVO_4$ photoanode significantly resulted in a narrower visible band gap with a high photocurrent, further employed for the PEC water splitting application. The following sections thoroughly investigated and discussed an underlying phenomenon for this superior performance.

2. Materials and methods

2.1. Fabrication of $TiVO_4$ thin film *via* spray pyrolysis

All chemicals used for the fabrication of $TiVO_4$ were purchased from Merck Life Science Products (UK) and used without further purification.

$TiVO_4$ photoanodes were prepared *via* spray pyrolysis. The solution was prepared by dissolving vanadium acetylacetonate, and titanium isopropoxide in 15 mL of ethanol with a total concentration of 0.05 M. Next, 0.05 mL of trifluoroacetate acid (99%) was added to the mixture. It was kept under stirring for 2 h to get a clear homogenous solution. The solution was employed in the spray pyrolysis system, which comprises a syringe pump (New Era Pump system NE-1000), an attached vortex, and an ultrasonic atomizer (Sonozap) assisted with a nozzle of 1 mm (diameter). In this process, the prepared spray droplets are transported to the substrate through an atomizing nozzle. The evaporation of the solvent within the spray droplets leads to the formation of a uniform coating on the substrate. The parameters of the spray pyrolysis were maintained as

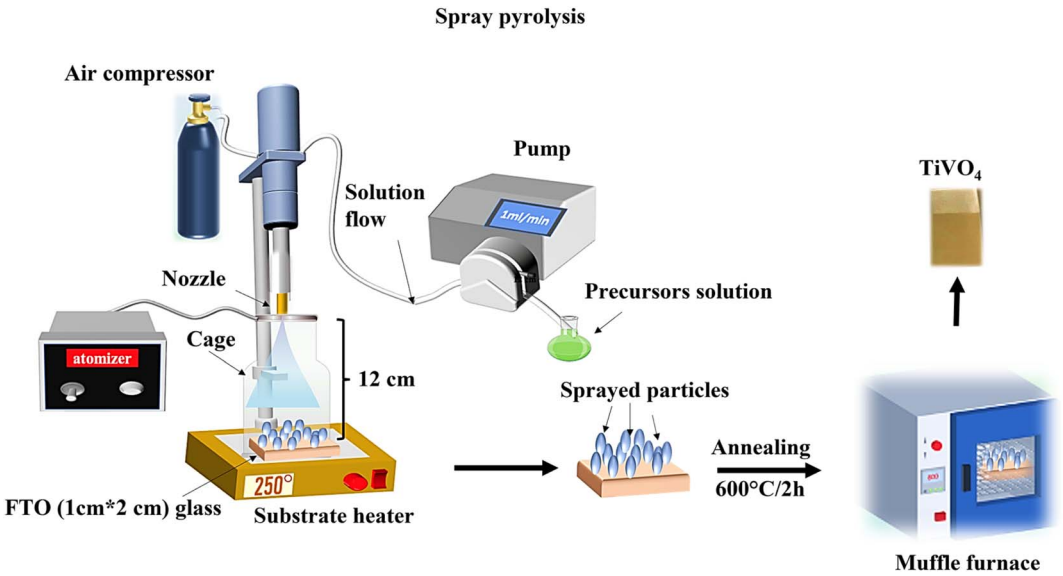

Fig. 1 Schematic representation of a $TiVO_4$ photoanode fabrication process using spray pyrolysis technique under optimised conditions.

follows, 10 mL of solution was sprayed on the 1 cm × 1 cm cleaned fluorine-doped tin oxide (FTO) glasses kept at a distance of 12 cm from the nozzle head at a flow rate of 1 mL min^{-1}, which is assisted with the compressed air (4 L min^{-1}). The deposition on the FTO glass was performed under various temperatures from 150 °C to 300 °C at an interval of 50 °C, referred to as substrate temperatures. Once the spray FTO finished, substrates were then taken for annealing at different temperatures from 500 °C to 650 °C, at an interval of 50 °C, for 2 h in a muffle furnace. The $TiVO_4$-coated FTO substrates were allowed to cool to room temperature before being taken for further analysis. Fig. 1 represents a schematic illustration of a $TiVO_4$ photoanode fabrication process using spray pyrolysis technique under optimised conditions.

2.2 Materials characterisations

Thin film microstructure analysis was performed using the TESCAN VEGA3 scanning electron microscopy (SEM) equipped with the energy dispersive spectroscopy (EDS) from Oxford Instruments. The structure and phases of the $TiVO_4$ thin films were characterised using a Bruker D8 X-ray diffractometer (XRD) assisted with a monochromatic CuK_α (λ = 0.154 nm) radiation. XPS Analysis was performed using a Thermo NEXSA XPS fitted with a monochromated Al K_α X-ray source (1486.7 eV). All sample data was recorded at a pressure below 10^{-8} Torr, and a room temperature of 294 K. Data was analysed using CasaXPS v2.3.20PR1.0 and calibrated with C 1s peak at 284.8 eV. Corresponding transmission electron microscopy (HR-TEM) analysis was carried out using JEOL JEM-2100F TEM (200 kV). The absorption and transmission spectra of the thin film were executed by PerkinElmer's UV-VIS-NIR UV-3600 Plus spectrophotometer.

$TiVO_4$ photoanode was employed for PEC studies, which were conducted utilising the Metrohm Autolab (PGSTAT302N) workstation consisting of three-electrode compartments. Where a platinum wire was used as the counter electrode, a 3 M aqueous solution of Ag/AgCl in KCl was considered the reference electrode, and 1 M aqueous solution of NaOH (pH of 13.6) was employed as the electrolyte for the electrochemical testing. The light intensity was simulated to achieve 1 SUN condition (100 mW cm^{-2}) from Newport, consisting of a 300 W xenon lamp with AM 1.5 filter and 420 nm cut-off filter to remove the UV part of the sunlight. The photoanode's voltages (potential *vs.* Ag/AgCl) were recorded at a scan rate of 0.01 V s^{-1} from negative to a positive potential direction (−0.3 V and +0.8) under light, dark and chopping conditions. All potentials were then converted to reversible hydrogen electrode (RHE) potential according to the Nernst eqn (1) as,

$$E_{RHE} = E_{Ag/AgCl} + 0.0591(pH) + 0.1976\ V \quad (1)$$

where the pH of the electrolyte was maintained at 13.6. Furthermore, the Mott–Schottky relationship was employed to determine the photoanode's flat band potential (V_{fb}).

3. Results and discussions

3.1. Structural and optical analysis

The XRD pattern of synthesized $TiVO_4$ photoanode exhibits single-phase material at 600 °C, as shown in Fig. 2a. The diffraction peaks correspond to 27.5°, 41.3° and 54.4°, representing the tetragonal lattice planes of (110), (111) and (211) for $TiVO_4$ structure. These results also corroborate with the JCPDS file 01-770332.[34] Besides, with almost similar intensity, the distinct peaks indicate FTO-glass substrate, and XRD confirms $TiVO_4$ thin film formation. No additional peaks of either TiO_2 or VO_2 hence admittedly manifested pure phase of $TiVO_4$ tetragonal structure. However, the XRD analysis was also performed at different substrate temperatures during the spray pyrolysis and further different annealing temperatures (Fig. S1, ESI†) to optimize the phase pure $TiVO_4$ thin film development. The optimized substrate and annealed temperatures were found to be 250 °C and 600 °C, respectively. Below these temperatures, either the tetragonal $TiVO_4$ phase does not entirely form, or the film deposition was not homogeneously covering the FTO surface; as a result, the XRD patterns revealed dominated peaks attributed to the FTO glass.

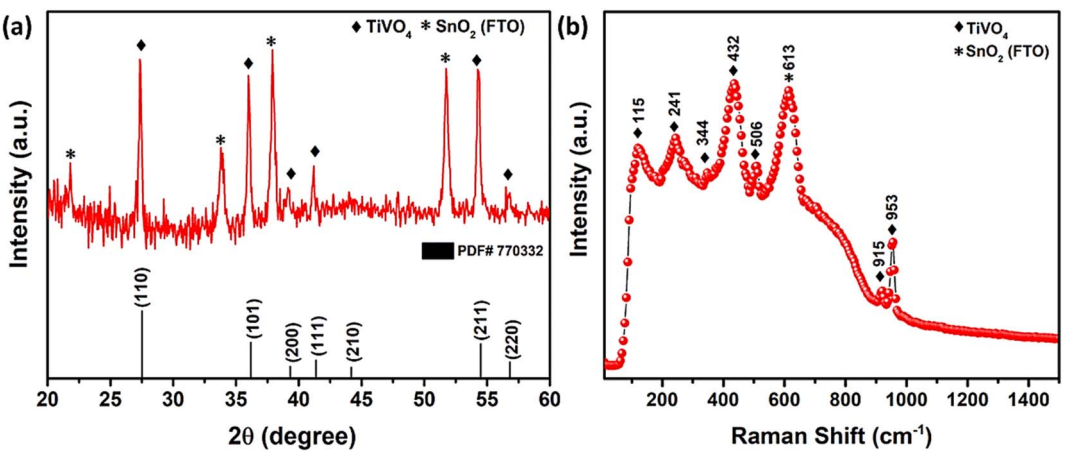

Fig. 2 (a) XRD pattern, (b) Raman spectrum of spray pyrolyzed $TiVO_4$ photoanode deposited on FTO glass.

Fig. 2b revealed the Raman spectrum of the optimized $TiVO_4$ thin film, confirming the successful formation of tetragonal $TiVO_4$ on the FTO glass. The stretching modes of V–O combining Ti–O and V–O occurred at higher wavenumber bands at ~915 and 953 cm^{-1}.[39] The bending and stretching modes appeared in the 400–600 cm^{-1} region. Other <400 cm^{-1} bands were external modes from the lattice, translational, and vibrational motions. Noticeably, Raman analysis of $TiVO_4$ (tetragonal) is rare; however, the concerning result has been compared with the $CrVO_4$ (orthorhombic) and $FeVO_4$ (triclinic) Raman bands relevant to $TiVO_4$.[40] It is anticipated that due to the difference in electronegativity of these metal, all the strongest peak of $TiVO_4$ exhibits a slightly lower intensity compared to $CrVO_4$ and $FeVO_4$. Also, because of its tetragonal and nondegenerate vibrations, the Raman bands of $TiVO_4$ were between $CrVO_4$ and $FeVO_4$. A peak at ~613 cm^{-1} corresponds to the A_{1g} vibrational mode of F-doped SnO_2 originating from the FTO glass.[41]

Fig. 3a–d reveals SEM microstructural images of $TiVO_4$ photoanode developed at different substrate temperatures of 150 °C, 200 °C, 250 °C and 300 °C, where the annealing temperature was maintained at 600 °C. The substrate temperature profoundly impacts the morphology and performance.[42–45] At lower substrate temperatures of 150 °C to 200 °C, the spray droplets splash directly onto the substrate (FTO) and decompose without evaporating the solvent in (Fig. 3a and b).[46] As a result, the particles agglomerated with an average size of ~700 nm, leaving bare FTO as shown in SEM (green coloured). This is due to the rapid droplet flux reaching the substrate without a complete nucleation growth process, leading to rough films and an ununiform distribution of the material on FTO glass. Whereas at the substrate temperature of 250 °C, the solvent will leave before reaching the substrate, and a solid precipitate of precursor will fall on the substrate providing a homogenous coating. As a result, growth is uniform, and the bead-like structure with reduced particle size narrowed down to 300 nm, securing better coverage and homogeneous deposition across the FTO glass, as shown in Fig. 3c. However, at 300 °C substrate temperature, the decomposition of precursor starts before reaching the substrate, resulting in less adhesion to the substrate and giving powder particles on the surface, which peel off during the annealing process leaving bare FTO as shown in (Fig. 3d) (green coloured).[47,48] Based on the morphology observed by SEM; it is clear that the optimum substrate spray temperature for uniform and smooth films was found to be 250 °C.

Fig. 3e–h displays the impact of the various annealing temperatures from 500 °C to 650 °C on the films deposited at a substrate temperature of 250 °C. The images from Fig. 3e–h show that the only significant difference in morphology of the films is observed on those annealed at 500 °C. The morphology at this annealing temperature shows the wide distribution of the particle's size ranging from 600 to 150 nm, whereas the morphology of all those films annealed at 550 to 650 °C shows almost similar size distribution and more uniform growth. As well as Fig. 3e and f indicate that particle boundaries are agglomerated. While once the annealed temperature rises to ≥600 °C, the particles are comparatively distinct. The increase in porosity found in the films can be attributed to increased temperature, and the film becomes denser without cracks at higher temperatures. The thermophoretic effect during the high and optimized substrate temperatures of the $TiVO_4$ particle deposition was explained through a schematic, as shown in Fig. 3i and j, respectively. The substrate temperatures determine the rate of particle formation and their homogenous distribution. The growth of particles and concerning coverage maximized at 250 °C, and calcination temperature governs the phase purity and morphology of the fabricated particles. At higher substrate temperatures, particles' supersaturation rate and mobility were expected to be high and therefore yielded higher nucleation rates. In contrast, higher mobility facilitates nucleation collision and different growth rates of individual

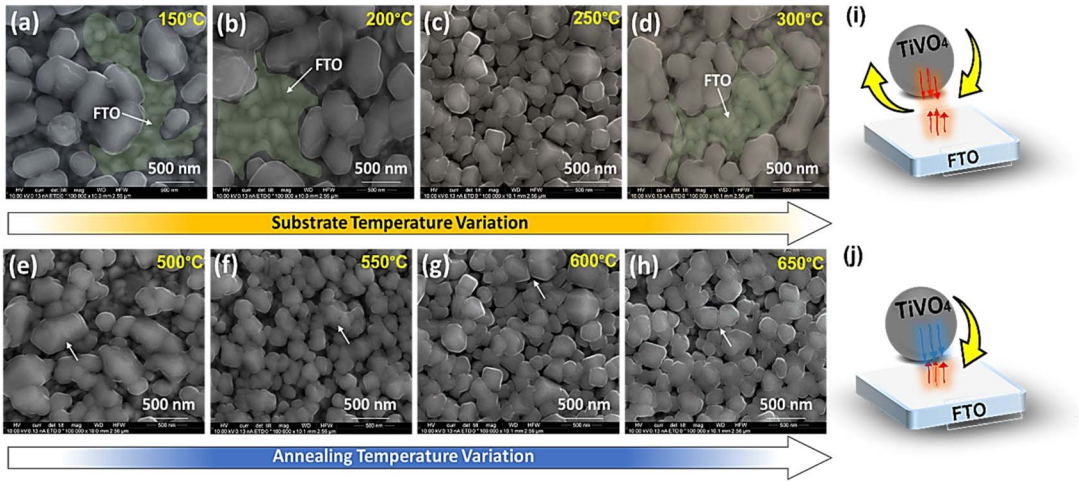

Fig. 3 SEM microstructural images of $TiVO_4$ photoanode at different substrate temperatures such as (a) 150 °C, (b) 200 °C, (c) 250 °C, (d) 300 °C where annealing temperature was fixed at 600 °C, and at different annealing temperatures such as (e) 500 °C (f) 550 °C (g) 600 °C (h) 650 °C, where the substrate temperature was fixed at 250 °C, respectively, schematic illustration of the thermophoretic effect of the (i) high substrate temperature of 300 °C and (j) optimized temperature of 250 °C on the particles deposition.

particles. Hence, by understanding the substrate and annealing temperature effect on morphology and homogeneity of the $TiVO_4$ photoanode, the optimised spray annealed temperatures are 250 °C, and 600 °C were taken for further analyses.

Furthermore, the high-resolution TEM was conducted to get detailed information and understand the nanostructured morphology and crystallinity of the $TiVO_4$. The TEM images shown in Fig. 4a display scattered nanoparticle assemblies of $TiVO_4$, leading to an average diameter of ~100 nm. The $TiVO_4$ particles exhibit porous features, with some dendrites on their outer edge. Nanoparticles have appeared to form some extent of designed agglomeration. Fig. 4b represents corresponding high-resolution TEM images and selected area diffraction patterns (HR-TEM) images in the inset, indicating the tetragonal lattice fringes match well with the (111), (200) and (110) crystal planes of $TiVO_4$, indicating the presence of Ti, V in the composite form. T EDS spectrum was measured to further confirm the doping of vanadium ions into the TiO_2 lattice, as shown in Fig. 4c and S2, ESI.† The spectrum demonstrates the distinct peaks corresponding to Ti ($K_{\alpha 1}$) and V ($K_{\alpha 1}$) with a ratio of Ti : V as 1 : 1 (16.4% and 16.0%), providing the composite to be formed as $TiVO_4$. Furthermore, elemental color mapping was also carried out, aimed to be a suitable technique to validate the presence of $TiVO_4$ onto the FTO glass as shown for the $TiVO_4$ thin film as shown in Fig. 4d. It shows the coexistence of Ti, V, Sn and O belonging to $TiVO_4$. This result further confirms the deposition of $TiVO_4$ onto the FTO glass.

As photoelectrochemical activities are surface-driven phenomena, to understand the oxidation state of the elements present on the outermost surface, the surface composition of the sample was analysed by XPS integrated peak area analysis as shown in Fig. 5. The XPS survey spectra of $TiVO_4$ photoanode indicates the presence of Ti 2p, V 2p and O 1s, without any impurity and successfully deposited on the FTO glass, indicated by Sn $3d_{3/2}$ peak as displayed in Fig. 5a. The XPS peaks at 458.7 eV and 464.5 eV corresponding to the binding energies of the Ti $2p_{3/2}$ and $2p_{1/2}$ (Fig. 5b). The spin–orbit splitting energy of 5.8 eV is the characteristic of Ti^{4+} oxidation state present in the $TiVO_4$ structure.[49] In addition, the Ti 2p core level spectra can be fitted into Ti^{3+} peaks at ~457.8 eV and ~461.6 eV corresponding to Ti^{3+} $2p_{3/2}$ and Ti^{3+} $2p_{1/2}$, originating due to the partial reduction of Ti^{4+} state by the generation of oxygen vacancies in the reducing atmosphere. It is reported that Ti^{3+} species and/or oxygen vacancies may significantly improve the observed electronic conductivity of the material.[50] However, compared to the Ti^{4+} oxidation state, the Ti^{3+} oxidation state is negligible.

There are strong hybridization between V 2p and O 1s states and thus exposed various oxidation states of V 2p during $TiVO_4$ formation. The peaks at 516.3 and 517.2 eV correspond to the binding energies of V $2p_{3/2}$ for V^{4+} and V^{5+}, respectively, as shown in Fig. 5c. Besides, the V $2p_{1/2}$ peaks are positioned at 524.4, and 523.1 eV corresponding to V^{5+} and V^{4+}.[51] V^{5+} might result from the surface oxidation of the samples in the air, which is common in vanadium-based samples.[52] The observed broadening of the V $2p_{3/2}$, the linewidth is due to the decrease of the oxidation state. As a result, V^{2+} peaks were also observed.[52] However, the formation of VO has the oxidation state V^{2+}, which is not reported in any previous study. Therefore we cannot unambiguously assign the third component to a vanadium oxidation state. The overlapped mixed-valence oxidation states of V^{5+} and V^{4+} are usually observed in ternary vanadium-based oxides.[53] Such overlapping peaks contain mixed valences of V^{5+} and V^{4+}. Also, the V_{2p} binding energies of $TiVO_4$ were lower than the bare V_2O_5 and VO_3 due to the ternary oxide composition. Eventually, the pristine of $TiVO_4$ show a ratio V/O ~0.27, in agreement with the ratio found in the $TiVO_4$ (0.25); thus, it is expected that only V^{4+} is present in the sample. The existence of V^{5+} species in the $TiVO_4$ thin film suggests that during the chemical synthesis, possible interactions of between the Ti–V sol produce a partial shift to higher binding energy in concordance with the V^{5+} species.

Further, two peaks for oxygen (O 1s) were observed, one for O^{2-} in the metal oxide as interaction strength of the V═O

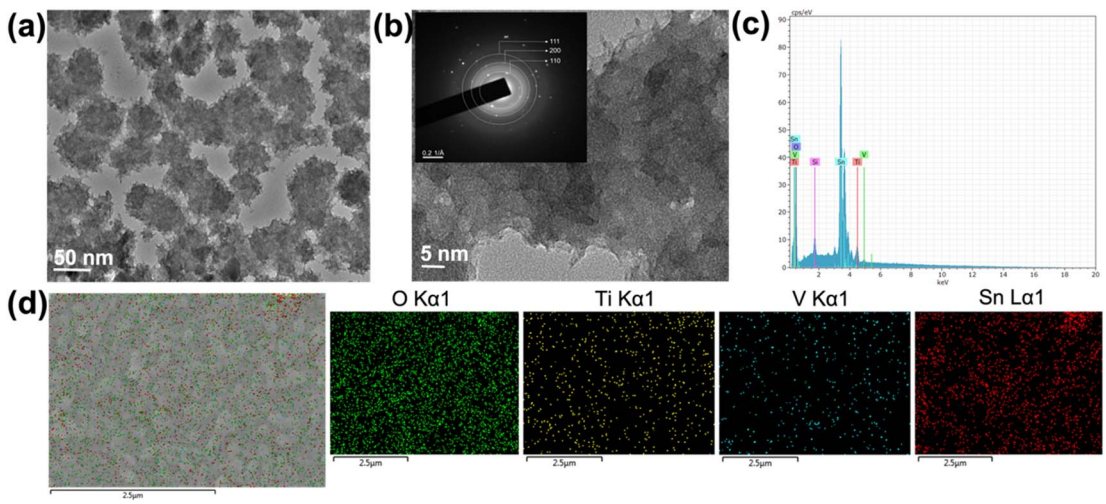

Fig. 4 (a) TEM bright field image, (b) corresponding HRTEM and SAED images (inset), (c) EDS spectrum and (d) corresponding element colour mapping of the $TiVO_4$ photoanode.

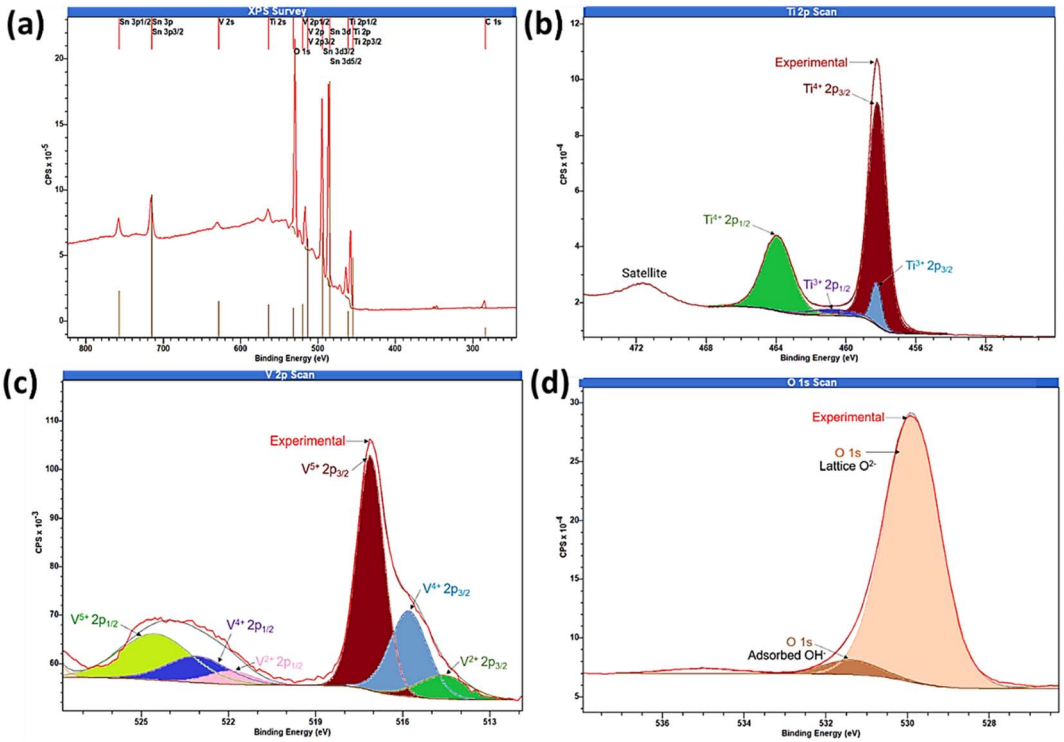

Fig. 5 X-ray photoelectron spectroscopy (a) survey spectrum and core level spectrum of (b) Ti 2p, (c) V 2p and (d) O 1s regions of $TiVO_4$ thin film deposited on a FTO glass.

bonds, and O═V–O–V^{4+}(V^{5+})–O–Ti^{4+} to form $TiVO_4$. While the other one at 532.2 eV characteristics of chemisorbed oxygen on transition-metal as shown in Fig. 5d.[54] The surface atomic percentages calculated from the XPS data were Ti 2p ~9%, V 2p ~8.2%, O 1s ~36% and Sn 3d ~4%. The elemental composition and distribution are corroborated with the XRD, EDS and XPS measurements. These results further proved that the nanostructures of $TiVO_4$ had been successfully grown on the surface of FTO glass.

Fig. 6a exhibits the transmittance spectra of the $TiVO_4$ photoanode and compares it with the FTO glass. The FTO glass shows an average transmittance of ~80%, whereas the $TiVO_4$ thin film exhibits slightly less steady transmittance to ~50. Reduction in transmittance indicates the formation of a thin film on FTO glass. During the spray pyrolysis process, the thin film retained semi-transparent behaviour for all the samples. This is also evident from the thin film's colour, which visually appears light yellow. During the spray pyrolysis process, the thin film retained semi-transparent behaviour for all the samples. This is also evident from the thin film's colour, which visually appears light yellow. Fig. 6b shows the maximum absorption edge of $TiVO_4$ ~ 400 nm, which shows an exponential decrease towards the visible wavelength region.

Moreover, the absorption edge of the composite has been extended to the visible region up to 600 nm due to incorporating V^{4+} in the TiO_2 structure, which could help harvest the UV and visible components of the solar radiation. The optical bandgap estimation was calculated using reflectance measurement from

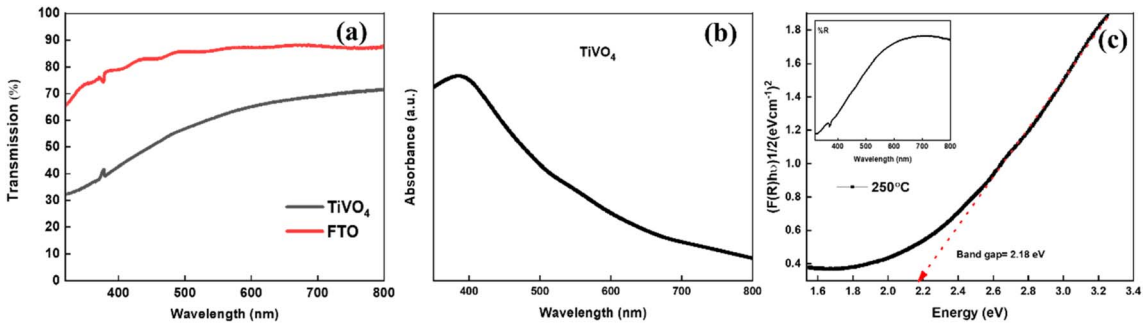

Fig. 6 (a) Transmittance spectra of $TiVO_4$ photoanode fabricated at an optimized substrate temperature 250 °C and calcined at 600 °C, compared with FTO, corresponding (b) absorption (c) reflectance spectra concerning the Kubelka–Monk plot, respectively.

the Kubelka Munk equation, as shown in Fig. 6c. The band gap of $TiVO_4$ is estimated to be ~2.18 eV. $TiVO_4$ bandgap was narrower than TiO_2, where V^{4+} incorporation plays a crucial role. This may be because the ionic radii of V^{4+} are 0.72 Å, which is close to the Ti^{4+} ionic radii (0.74 Å), which signifies interstitial doping of V^{4+} within TiO_2 lattice TiO_2 enables tuning its light-absorbing capacity. Narrowing the wide bandgap indicates $TiVO_4$ could be used as an anodic electrode for water-splitting applications.

3.2. Photoelectrochemical analysis

Considering the optical analysis, nanostructure, and phase pure properties, the fabricated $TiVO_4$ photoanodes were employed for PEC investigation with varied substrate and annealing temperatures. The linear sweep voltage (LSV) plot (Fig. 7a), *i.e.*, photocurrent (μA) *vs.* potential (*vs.* Ag/AgCl), was performed at a scan rate of 1 mV s^{-1} of the $TiVO_4$ as a working electrode was recorded under chopped conditions (light and dark with chopping at an interval of 0.2 V *vs.* Ag/AgCl) for various substrate temperatures fabricated films. Among the various substrate temperatures, the photoanode developed at 250 °C recorded the highest photocurrent of 400 μA at 0.8 V *vs.* Ag/AgCl (1.8 V *vs.* RHE), which is much higher than the other samples sprayed at 150 °C (108 μA), 200 °C (135 μA) and 300 °C (145 μA). Fig. 7b indicates the trend of photocurrent obtained by the $TiVO_4$ photoanode developed at various substrate temperatures at 1.4 and 1.8 V *vs.* RHE. The photocurrent slightly increases with an increase in temperature from 150 to 200 °C, *i.e.*, from 108 to 135 μA. Intermediate adhesion and incomplete phase development with low coverage of the particles on FTO glass could have resulted in low photocurrent.[55] At 250 °C, it drastically enhanced to 400 μA. This phenomenon is mainly attributed to the sufficient temperature required to evaporate the organic materials, forming the pure phase material. At an optimised substrate temperature, maximum nucleation density and proper atomic diffusion can be achieved, resulting in the material's complete growth.[56,57] However, at 300 °C, the photocurrent decreases significantly beyond this temperature to 140 μA. This is ascribed to the agglomeration and decomposition of the materials at higher temperatures and corroborates with the SEM data. The overall trend of photocurrent generation for different substrate temperatures was followed as 150 °C < 200 °C ~250 °C > 300 °C.

Next, to evaluate the effect of different annealing temperatures on the $TiVO_4$ photoanodes, the LSV photocurrent transients were obtained, as shown in Fig. 7c. Here, the substrate temperature was maintained at the optimized temperature, *i.e.*, 250 °C. A significant enhancement in the photocurrent is noticed for the thin film annealed at 600 °C. The photocurrent seemed to increase monotonically from 73 to 400 μA with an increase in annealing temperature from 500 to 600 °C. This was due to better coverage on the substrate, uniformity of the thin film as observed by SEM, and improved crystallinity improvement as confirmed by XRD. The overall trend of photocurrent generation for different substrate temperatures was followed as 500 °C < 550 °C < 600 °C > 650 °C. The trend for photocurrent

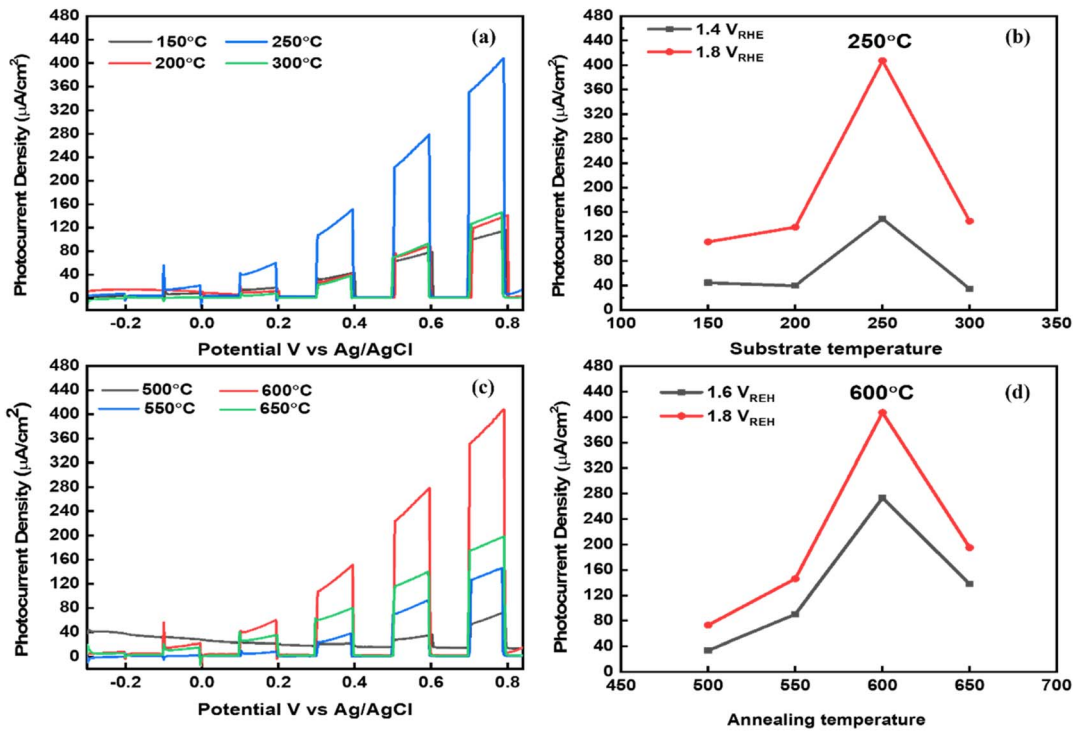

Fig. 7 Linear sweep voltammetry (LSV of current density – potential *vs.* Ag/AgCl) plots under 100 mW cm^{-2} chopped light and dark illumination at a scan rate of 0.2 mV s^{-1} in 1 M NaOH electrolyte (pH = 13.6) showing (a and b) effect of substrate temperatures and (c and d) annealing temperatures on the PEC performance.

achievement at different annealing temperatures at 1.4 and 1.8 V *vs.* RHE was further described in Fig. 7d. Nevertheless, higher annealing temperature (650 °C) displays a drop in the photocurrent to 196 μA, primarily due to the increasing its overall resistivity of films which may be due to the sintering of particles to the increased size and reduce the surface area.[58]

The linear sweep voltammogram (LSV) of the optimised $TiVO_4$ photoanode was plotted in Fig. 8a and measured under dark and illumination conditions with an onset potential of ~0.8 V (*vs.* RHE). Herein, the photocurrent was significantly increased over the positive potential scan range, which indicates that $TiVO_4$ is working as an effective photoanode material. At the bias potential of 1.8 V *vs.* RHE, photocurrent density was measured to be the highest value of 400 μA cm^{-2}. Also, the stability of optimised $TiVO_4$ was investigated using the chronoamperometry technique by keeping the film under illumination at a maintained applied bias potential of 0.23 V *vs.* Ag/AgCl (1.23 V *vs.* RHE), representing the required PEC water potential for 6000 s Fig. 8b. Steady-state of photocurrent density was extrapolated over tested time without degradation of the total of photocurrent density. Furthermore, to investigate the charge transport kinetics of the $TiVO_4$, electrochemical impedance measurements were carried out under both dark and 1 SUN illumination (100 mW cm^{-2}). The Nyquist plots of electrochemical impedance spectra of obtained data are shown in Fig. 8c, with an equivalent circuit ($R_1 + R_2/C_2 + R_3/C_3$) in the inset used to evaluate resistance values. R_1 represents the total solution resistances of the circuit among FTO, titanium vanadate film and connecting wires, R_2 is a resistance that arises from charge transfer at the electrode/electrolyte interface, and R_3 represents the resistance of charge transport of the bulk $TiVO_4$ film.[59] Simultaneously, C_2 and C_3 are ascribed to the bulk material's capacitance and the associated surface states. Under light conditions, resistance values of R_1, R_2 and R_3 were found to be 12.41 Ω, 1983 Ω and 113 Ω, respectively, indicating the facile charge transfer of the obtained film and thus promoting PEC activity.

The Mott–Schottky calculation was carried out to determine the space-charge capacitance over potential scan ranges and the flat band potential of the optimized photoanode. The Mott–Schottky plot elucidated the n-type performance of $TiVO_4$ film, as shown in Fig. 8d. Flat band potential was estimated to be −0.26 V *vs.* Ag/AgCl and used in the Mott–Schottky eqn (2) to calculate the concentration of the dopants (N_D)

$$\left(\frac{1}{C}\right)^2 = \frac{2}{\varepsilon_r \varepsilon_0 A^2 e N_D}\left(V - V_{fb} - \frac{K_B T}{e}\right) \quad (2)$$

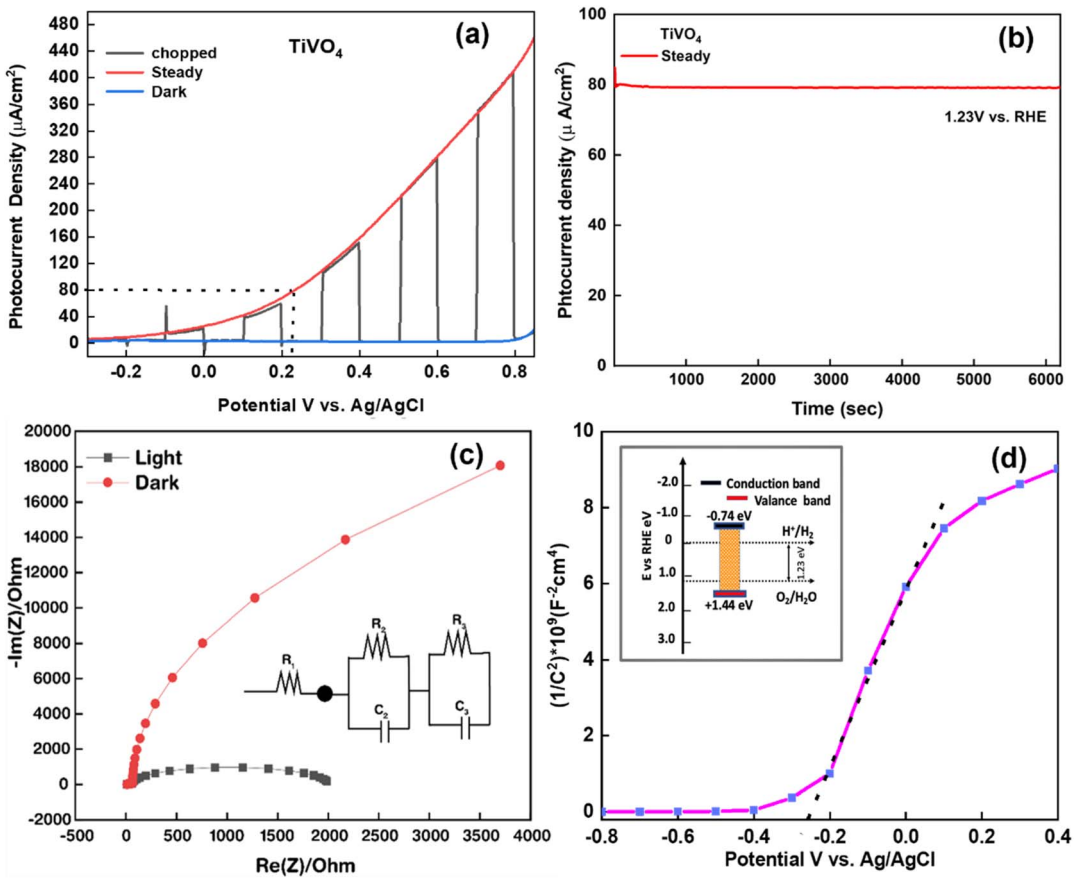

Fig. 8 (a) LSV curves of optimized $TiVO_4$ film under light–dark-chopped conditions (b) photocurrent stability plot under continuous 1 SUN illumination for 12 h (c) electrochemical impedance spectroscopy data obtained for $TiVO_4$ photoanode under dark–light condition (circuit diagram shown in the inset) (d) Mott Schottky data are showing the flat band potentials.

Table 1 Comparative study of $TiVO_4$ photoanode with the latest developed thin films *via* spray pyrolysis for PEC study

Serial no.	Sample	Fabrication/deposition technique	Highest photocurrent (mA cm^{-2}) (at 1.23 V *vs.* RHE)	Stability tested time (h)	Reference
1	$LaFeO_3$	Spray pyrolysis	0.0180	21	61
2	Bi_2WO_6	Spray pyrolysis	0.042	—	62
3	$BiFeO_3$	Spray pyrolysis	0.012	—	63
4	$ZnFe_2O_4$	Spray pyrolysis	0.130	1.37	64
5	$TiVO_4$	Spray pyrolysis	0.080	1.66	This study

where C is space-charge capacitance, ε_0 is the permittivity of vacuum, ε_r is the relative permittivity of a material, A is the area of the film, N_D is the carrier concentration, K_B is Boltzmann constant, T is temperature, e is the electronic charge, V is applied potential and V_{fb} is the flat band potential which is estimated through linear fit in Mott–Schottky plot. The slope was measured to be 5.6×10^9, and the carrier density was calculated to be 7.7×10^{20} cm^{-3}. The two bands' positions of the valence band (+1.44 V *vs.* RHE) and conduction band (−0.74 V *vs.* RHE) illustrated in Fig. 8d cover the required redox potentials to drive solar water splitting through the system. Estimated flat band potential refers to the conduction band of the film, as shown in the inset. Finally, this data may elucidate that the composition of $TiVO_4$ capable of producing hydrogen energy from the PEC water-splitting process.

In order to explain the overall water splitting in a PEC with an n-type semiconductor $TiVO_4$ photoanode, hydrogen is generated at the cathode while oxygen is evolved at the photoanode surface. Thus, the reaction products can be collected in separate chambers. In PEC water splitting, similar to the basic principle of photoanode, *i.e.*, on light irradiation, photoexcitation of the charge carriers followed by their migration to the photoanode surface take place. These photo-generated electrons (e^-) and holes (h^+) that migrate to the surface of the photocatalyst without recombination can produce gaseous hydrogen and oxygen, respectively, by reducing and/or oxidizing the water molecules, respectively adsorbed on the photoanode surface. The photo-oxidation of H_2O by the holes in the valence band causes a surface back reaction which demerits the H_2 evolution rate.

In this work, the narrow band gap of the obtained film at ~2.18 eV is suitable to absorb a wide range of incident visible light and thus form electron–hole pairs. The generated charge carries participation into the electrolyte with the species of O_2 and $OH^\bullet$ to trigger redox reactions. In brief, photo-generated electrons on the photoanode travel towards FTO, drifting to the cathode surface to carry out the reduction process (H_2 evolution).[60] Most importantly, some energy losses may occur due to recombining charge carriers, resulting in low photocurrent density. Next, photo-generated holes remain on the photoanode and usually experience slow kinetics at the interface between photoanode/electrolyte, resulting in hole accumulation, causing charge recombination, thus initiating oxygen evolution. The photoanode of the titanium vanadate film has shown enhanced PEC activity with lower charge transfer resistance observed from the impedance data than in the binary oxide of TiO_2 and VO_2 films.[6,15]

In addition, the higher photocurrent density of $TiVO_4$ lead to a promising alternative for the PEC application in future, and the observed data has been compared with the other reported materials in Table 1. Impressive photocurrent density and stability tested time were observed for the $TiVO_4$ photoanode compared with the other reported thin films developed *via* spray pyrolysis.

Although significant improvements have been achieved in the construction of highly efficient ternary $TiVO_4$ PEC materials, the recombination rate of photo-generated charge carriers for $TiVO_4$-based photocatalysts is still considerably high, accounting for poor reduction ability in the photoexcited electrons at a low potential of the conduction band edge, which is efficiently quenched by defects and holes. Morphological engineering could improve the PEC activity of $TiVO_4$, regulating the crystal structure, particle size, and surface area leading to a large-scale preparation, which would enormously improve the separation efficiency of the photo-generated charge carriers. Further, $TiVO_4$ could pave the way as a promising not only for PEC but also for smart coating and energy conversion.

4. Conclusion

This work describes the development of single-phase tetragonal nanostructure $TiVO_4$, which is not explored as a PEC material. $TiVO_4$ photoanode on FTO glass was fabricated using the scalable spray pyrolysis technique, a simple and efficient synthesis route showing a semi-transparent characteristic with a band gap of ~2.18 eV. XRD, Raman and XPS spectroscopic analysis confirms the formation of tetragonal phase pure $TiVO_4$ on an FTO glass. The development of $TiVO_4$ photoanode was studied for various substrate and annealing temperatures. The SEM microstructure analyses revealed the temperature effect of the $TiVO_4$ photoanode development. The optimized substrate temperature was found at 250 °C; the annealed temperature was 600 °C to achieve a single-phase $TiVO_4$ photoanode. The TEM analyses signify that the homogeneous distribution of $TiVO_4$ nanoparticles' agglomeration formed a dendritic outer edge fashion. The highest photocurrent density at 1.8 V *vs.* RHE of $TiVO_4$ was recorded at 400 μA cm^{-2} for the substrate temperature at 250 °C. Additionally, a narrower band gap (2.18 eV) of n-type semiconductor $TiVO_4$ makes it a beneficial light absorber, thus driving PEC water splitting for hydrogen generation. These results further inspire $TiVO_4$ employment as a photoanode

material with a particular emphasis on their applications in PEC solar water splitting under 1 SUN.

Furthermore, sprayed $TiVO_4$ photoanode showed excellent stability up to 6000 s. Besides, the photocurrent density monotonically improved from 73 to 400 μA cm^{-2} at 1.8 V *vs.* RHE with an increase in annealing temperature from 500 to 600 °C. Thus, the underlying photo-absorbing semiconductors could be fulfilled the lack of efficient photoanodes for the water-splitting reactions while not compromising either material's performance and achieving long-term passivation.

Conflicts of interest

There are no conflicts to declare.

Acknowledgements

This work was supported by Engineering and Physical Sciences Research Council (EPSRC) under the research grant no. EP/V049046/1. MA would like to acknowledge the financial support from the Saudi Arabia Culture Bureau in the United Kingdom. The X-ray photoelectron (XPS) data collection was performed at the EPSRC National Facility for XPS ("HarwellXPS"), operated by Cardiff University and UCL, under Contract No. PR16195. The authors acknowledge the help rendered for the SEM and TEM characterizations by Dr Hong Chang, Imaging Suite Manager, Harrison Building, University of Exeter, Streatham Campus, U.K.

References

1 R. Van de Krol and M. Grätzel, *Photoelectrochemical hydrogen production*, Springer, 2012.
2 Y. Wang, J. Zhang, M.-S. Balogun, Y. Tong and Y. Huang, Oxygen vacancy-based metal oxides photoanodes in photoelectrochemical water splitting, *Mater. Today Sustain.*, 2022, **18**, 100118.
3 H. Shi, H. Guo, S. Wang, G. Zhang, Y. Hu, W. Jiang and G. Liu, Visible Light Photoanode Material for Photoelectrochemical Water Splitting: A Review of Bismuth Vanadate, *Energy Fuels*, 2022, **36**(19), 11404–11427.
4 S. Li, W. Xu, L. Meng, W. Tian and L. Li, Recent Progress on Semiconductor Heterojunction-Based Photoanodes for Photoelectrochemical Water Splitting, *Small Sci.*, 2022, 2100112.
5 A. R. Fareza, F. A. A. Nugroho, F. Abdi and V. Fauzia, Nanoscale metal oxides-2D materials heterostructures for photoelectrochemical water splitting—a review, *J. Mater. Chem. A*, 2022, **10**, 8656–8686.
6 A. Fujishima and K. Honda, Electrochemical photolysis of water at a semiconductor electrode, *Nature*, 1972, **238**, 37–38.
7 D. Bae, B. Seger, P. C. Vesborg, O. Hansen and I. Chorkendorff, Strategies for stable water splitting *via* protected photoelectrodes, *Chem. Soc. Rev.*, 2017, **46**, 1933–1954.
8 R. Abe, Recent progress on photocatalytic and photoelectrochemical water splitting under visible light irradiation, *J. Photochem. Photobiol., C*, 2010, **11**, 179–209.
9 Q. Huang, Z. Ye and X. Xiao, Recent progress in photocathodes for hydrogen evolution, *J. Mater. Chem. A*, 2015, **3**, 15824–15837.
10 Y. Tachibana, L. Vayssieres and J. R. Durrant, Artificial photosynthesis for solar water-splitting, *Nat. Photonics*, 2012, **6**, 511–518.
11 A. A. Tahir, K. U. Wijayantha, S. Saremi-Yarahmadi, M. Mazhar and V. McKee, Nanostructured α-Fe_2O_3 thin films for photoelectrochemical hydrogen generation, *Chem. Mater.*, 2009, **21**, 3763–3772.
12 T. Hong, Z. Liu, X. Zheng, J. Zhang and L. Yan, Efficient photoelectrochemical water splitting over Co_3O_4 and Co_3O_4/Ag composite structure, *Appl. Catal., B*, 2017, **202**, 454–459.
13 S. Hoang, S. P. Berglund, N. T. Hahn, A. J. Bard and C. B. Mullins, Enhancing visible light photo-oxidation of water with TiO_2 nanowire arrays *via* cotreatment with H_2 and NH_3: synergistic effects between Ti^{3+} and N, *J. Am. Chem. Soc.*, 2012, **134**, 3659–3662.
14 J. Bullock, A. Cuevas, T. Allen and C. Battaglia, Molybdenum oxide MoO_x: a versatile hole contact for silicon solar cells, *Appl. Phys. Lett.*, 2014, **105**, 232109.
15 I. N. Reddy, A. Sreedhar, J. Shim and J. S. Gwag, Multifunctional monoclinic VO_2 nanorod thin films for enhanced energy applications: photoelectrochemical water splitting and supercapacitor, *J. Electroanal. Chem.*, 2019, **835**, 40–47.
16 E. A. Gibson, L. Le Pleux, J. Fortage, Y. Pellegrin, E. Blart, F. Odobel, A. Hagfeldt and G. Boschloo, Role of the triiodide/iodide redox couple in dye regeneration in p-type dye-sensitized solar cells, *Langmuir*, 2012, **28**, 6485–6493.
17 H. M. Chen, C. K. Chen, Y. C. Chang, C. W. Tsai, R. S. Liu, S. F. Hu, W. S. Chang and K. H. Chen, Quantum dot monolayer sensitized ZnO nanowire-array photoelectrodes: true efficiency for water splitting, *Angew. Chem.*, 2010, **122**, 6102–6105.
18 D. Carballeda-Galicia, R. Castanedo-Perez, O. Jimenez-Sandoval, S. Jimenez-Sandoval, G. Torres-Delgado and C. Zuniga-Romero, High transmittance CdO thin films obtained by the sol–gel method, *Thin Solid Films*, 2000, **371**, 105–108.
19 Q. Ding, L. Gou, D. Wei, D. Xu, W. Fan and W. Shi, Metal–organic framework derived Co_3O_4/TiO_2 heterostructure nanoarrays for promote photoelectrochemical water splitting, *Int. J. Hydrogen Energy*, 2021, **46**, 24965–24976.
20 Y. Fu, *et al.*, A ternary nanostructured α-Fe_2O_3/Au/TiO_2 photoanode with reconstructed interfaces for efficient photoelectrocatalytic water splitting, *Appl. Catal., B*, 2020, **260**, 118206.
21 Y.-K. Hsu, Y.-C. Chen and Y.-G. Lin, Novel ZnO/Fe_2O_3 core–shell nanowires for photoelectrochemical water splitting, *ACS Appl. Mater. Interfaces*, 2015, **7**, 14157–14162.
22 M. Alhabradi, S. Nundy, A. Ghosh and A. A. Tahir, Vertically Aligned CdO-Decked α-Fe_2O_3 Nanorod Arrays by a Radio

Frequency Sputtering Method for Enhanced Photocatalytic Applications, *ACS Omega*, 2022, **7**(32), 28396–28407.

23 D. Bae, G. Kanellos, K. Wedege, E. Dražević, A. Bentien and W. A. Smith, Tailored energy level alignment at MoOX/GaP interface for solar-driven redox flow battery application, *J. Chem. Phys.*, 2020, **152**, 124710.

24 P. Sahoo, A. Sharma, S. Padhan and R. Thangavel, Construction of ZnO@NiO heterostructure photoelectrodes for improved photoelectrochemical performance, *Int. J. Hydrogen Energy*, 2021, **46**, 36176–36188.

25 Z. Dong, D. Ding, T. Li and C. Ning, Ni-doped TiO_2 nanotubes photoanode for enhanced photoelectrochemical water splitting, *Appl. Surf. Sci.*, 2018, **443**, 321–328.

26 M. Altomare, K. Lee, M. S. Killian, E. Selli and P. Schmuki, Ta-doped TiO_2 nanotubes for enhanced solar-light photoelectrochemical water splitting, *Chem.–Eur. J.*, 2013, **19**, 5841–5844.

27 C. Cheng and Y. Sun, Carbon doped TiO_2 nanowire arrays with improved photoelectrochemical water splitting performance, *Appl. Surf. Sci.*, 2012, **263**, 273–276.

28 S. Hernández, S. M. Thalluri, A. Sacco, S. Bensaid, G. Saracco and N. Russo, Photo-catalytic activity of $BiVO_4$ thin-film electrodes for solar-driven water splitting, *Appl. Catal., A*, 2015, **504**, 266–271.

29 H. Mandal, S. Shyamal, P. Hajra, A. Bera, D. Sariket, S. Kundu and C. Bhattacharya, Development of ternary iron vanadium oxide semiconductors for applications in photoelectrochemical water oxidation, *RSC Adv.*, 2016, **6**, 4992–4999.

30 S. S. Kalanur and H. Seo, Facile growth of compositionally tuned copper vanadate nanostructured thin films for efficient photoelectrochemical water splitting, *Appl. Catal., B*, 2019, **249**, 235–245.

31 Q. Jia, K. Iwashina and A. Kudo, Facile fabrication of an efficient $BiVO_4$ thin film electrode for water splitting under visible light irradiation, *Proc. Natl. Acad. Sci. U. S. A.*, 2012, **109**, 11564–11569.

32 D. Mei, L. Li, C. Zhu, X. Zhao and Y. Yuan, Phy-chemical Attributes of Nano-scale V_2O_5/TiO_2 Catalyst and Its' Effect on Soot Oxidation, *Bull. Chem. React. Eng. Catal.*, 2016, **11**, 161–169.

33 K. Y. Jung, Y. R. Jung, J.-K. Jeon, J. H. Kim and Y.-K. Park, Catalytic conversion of 1,2-dichlorobenzene over mesoporous V_2O_5/TiO_2 prepared from spray pyrolysis, *J. Nanosci. Nanotechnol.*, 2011, **11**, 1710–1713.

34 A. Tripathi, R. G. Nair and S. Samdarshi, Visible active silver sensitized vanadium titanium mixed metal oxide photocatalyst nanoparticles through sol–gel technique, *Sol. Energy Mater. Sol. Cells*, 2010, **94**, 2379–2385.

35 A. Wren, B. Adams, D. Pradhan, M. Towler and N. Mellott, Titanium–vanadium oxide nanocomposite thin films: synthesis, characterization and antibacterial activity, *Mater. Chem. Phys.*, 2014, **144**, 538–546.

36 P.-Y. Zhou, C.-C. Cheng, C.-H. Huang and J.-K. Chen, Hexagonal pillar structure of heteroepitaxial titania–vanadia nanocrystal films for high performance in thermochromic and photocatalytic properties, *Phys. Chem. Chem. Phys.*, 2016, **18**, 9088–9101.

37 H. Liu, X. Wang, Z. Lan and H. Xu, Titanium Vanadium Oxide Thin Films Prepared by Thermal Oxidation of Titanium–Vanadium Alloy as Photocatalyst for Methylene Blue Degradation under Visible Light, *J. Mater. Eng. Perform.*, 2021, **30**, 1711–1722.

38 X. Jin, W. Sun, C. Chen, T. Wei, Y. Cheng, P. Li and Q. Li, Efficiency enhancement *via* tailoring energy level alignment induced by vanadium ion doping in organic/inorganic hybrid solar cells, *RSC Adv.*, 2014, **4**, 46008–46015.

39 X. He, C. Zhang and D. Tian, The structure, vibrational spectra, and thermal expansion study of AVO_4 (A = Bi, Fe, Cr) and $Co_2V_2O_7$, *Materials*, 2020, **13**, 1628.

40 G. Bera, V. Reddy, P. Rambabu, P. Mal, P. Das, N. Mohapatra, G. Padmaja and G. Turpu, Triclinic–monoclinic–orthorhombic (T–M–O) structural transitions in phase diagram of $FeVO_4$–$CrVO_4$ solid solutions, *J. Appl. Phys.*, 2017, **122**, 115101.

41 X. Wang, X. Wang, Q. Di, H. Zhao, B. Liang and J. Yang, Mutual effects of fluorine dopant and oxygen vacancies on structural and luminescence characteristics of F doped SnO_2 nanoparticles, *Materials*, 2017, **10**, 1398.

42 F. Zahedi, R. Dariani and S. Rozati, Effect of substrate temperature on the properties of ZnO thin films prepared by spray pyrolysis, *Mater. Sci. Semicond. Process.*, 2013, **16**, 245–249.

43 A. Bouzidi, N. Benramdane, H. Tabet-Derraz, C. Mathieu, B. Khelifa and R. Desfeux, Effect of substrate temperature on the structural and optical properties of MoO_3 thin films prepared by spray pyrolysis technique, *Mater. Sci. Eng., B*, 2003, **97**, 5–8.

44 R. Irani, S. Rozati and S. Beke, Structural and optical properties of nanostructural V_2O_5 thin films deposited by spray pyrolysis technique: effect of the substrate temperature, *Mater. Chem. Phys.*, 2013, **139**, 489–493.

45 A. A. Tahir, M. A. Ehsan, M. Mazhar, K. U. Wijayantha, M. Zeller and A. Hunter, Photoelectrochemical and photoresponsive properties of Bi_2S_3 nanotube and nanoparticle thin films, *Chem. Mater.*, 2010, **22**, 5084–5092.

46 D. Perednis and L. J. Gauckler, Thin film deposition using spray pyrolysis, *J. Electroceram.*, 2005, **14**, 103–111.

47 A. Tricoli and T. D. Elmøe, Flame spray pyrolysis synthesis and aerosol deposition of nanoparticle films, *AIChE J.*, 2012, **58**, 3578–3588.

48 A. B. Khatibani and S. Rozati, Synthesis and characterization of amorphous aluminum oxide thin films prepared by spray pyrolysis: effects of substrate temperature, *J. Non-Cryst. Solids*, 2013, **363**, 121–133.

49 A. Roy, S. Mukhopadhyay, P. S. Devi and S. Sundaram, Polyaniline-layered rutile TiO_2 nanorods as alternative photoanode in dye-sensitized solar cells, *ACS Omega*, 2019, **4**, 1130–1138.

50 L. Wang, *et al.*, Structural and electrochemical characteristics of Ca-doped "flower-like" $Li_4Ti_5O_{12}$ motifs as high-rate anode materials for lithium-ion batteries, *Chem. Mater.*, 2018, **30**, 671–684.

51 J. Wang, X. Zhang, Y. Zhang, A. Abas, X. Zhao, Z. Yang, Q. Su, W. Lan and E. Xie, Lightweight, interconnected VO_2 nanoflowers hydrothermally grown on 3D graphene networks for wide-voltage-window supercapacitors, *RSC Adv.*, 2017, **7**, 35558–35564.

52 G. Silversmit, D. Depla, H. Poelman, G. B. Marin and R. De Gryse, Determination of the V 2p XPS binding energies for different vanadium oxidation states (V^{5+} to V^{0+}), *J. Electron Spectrosc. Relat. Phenom.*, 2004, **135**, 167–175.

53 X. Zhao, Y. Yan, L. Mao, M. Fu, H. Zhao, L. Sun, Y. Xiao and G. Dong, A relationship between the V^{4+}/V^{5+} ratio and the surface dispersion, surface acidity, and redox performance of V_2O_5–WO_3/TiO_2 SCR catalysts, *RSC Adv.*, 2018, **8**, 31081–31093.

54 A. Roy, S. Bhandari, A. Ghosh, S. Sundaram and T. K. Mallick, Incorporating solution-processed mesoporous WO_3 as an interfacial cathode buffer layer for photovoltaic applications, *J. Phys. Chem. A*, 2020, **124**, 5709–5719.

55 R. Swapna and M. S. Kumar, The role of substrate temperature on the properties of nanocrystalline Mo doped ZnO thin films by spray pyrolysis, *Ceram. Int.*, 2012, **38**, 3875–3883.

56 T. S. Rao, C. Halpin, J. Webb, J. Noad and J. McCaffrey, Effect of substrate temperature on the growth rate and surface morphology of heteroepitaxial indium antimonide layers grown on (100) GaAs by metalorganic magnetron sputtering, *J. Appl. Phys.*, 1989, **65**, 585–590.

57 M. Mousavi, A. Kompany, N. Shahtahmasebi and M. Bagheri-Mohagheghi, Study of structural, electrical and optical properties of vanadium oxide condensed films deposited by spray pyrolysis technique, *Adv. Manuf.*, 2013, **1**, 320–328.

58 G. Rahman and O.-S. Joo, Photoelectrochemical water splitting at nanostructured α-Fe_2O_3 electrodes, *Int. J. Hydrogen Energy*, 2012, **37**, 13989–13997.

59 S. S. Kalanur, Y. J. Lee and H. Seo, Exploring the synthesis, band edge insights, and photoelectrochemical water splitting properties of lead vanadates, *ACS Appl. Mater. Interfaces*, 2021, **13**, 25906–25917.

60 Z. Chen, H. N. Dinh and E. Miller, *Photoelectrochemical water splitting*, Springer, 2013.

61 G. S. Pawar and A. A. Tahir, Unbiased spontaneous solar fuel production using stable $LaFeO_3$ photoelectrode, *Sci. Rep.*, 2018, **8**, 1–9.

62 B. Y. Alfaifi, A. A. Tahir and K. U. Wijayantha, Fabrication of Bi_2WO_6 photoelectrodes with enhanced photoelectrochemical and photocatalytic performance, *Sol. Energy Mater. Sol. Cells*, 2019, **195**, 134–141.

63 G. Liu, S. K. Karuturi, H. Chen, D. Wang, J. W. Ager, A. N. Simonov and A. Tricoli, Enhancement of the photoelectrochemical water splitting by perovskite $BiFeO_3$ *via* interfacial engineering, *Sol. Energy*, 2020, **202**, 198–203.

64 J. W. Park, *et al.*, Activation of a highly oriented columnar structure of $ZnFe_2O_4$ for photoelectrochemical water splitting: orchestrated effects of two-step quenching and Sn^{4+} diffusion, *Sol. Energy Mater. Sol. Cells*, 2018, **187**, 207–218.